



Article

# Preparation of High-Porosity B-TiO<sub>2</sub>/C<sub>3</sub>N<sub>4</sub> Composite Materials: Adsorption–Degradation Capacity and Photo-Regeneration Properties

Xiang Guo <sup>1</sup>, Lei Rao <sup>2,\*</sup> and Zhenyu Shi <sup>1</sup>

<sup>1</sup> College of Environment, Hohai University, Nanjing 210098, China; gx2015@hhu.edu.cn (X.G.); szy@hhu.edu.cn (Z.S.)

<sup>2</sup> College of Mechanics and Materials, Hohai University, Nanjing 211100, China

\* Correspondence: rao@hhu.edu.cn

**Abstract:** Adsorption can quickly remove pollutants in water, while photocatalysis can effectively decompose organic matter. B-TiO<sub>2</sub>/g-C<sub>3</sub>N<sub>4</sub> ternary composite photocatalytic materials were prepared by molten method, and their adsorption–degradation capability under visible light conditions was discussed. The morphology of the B-TiO<sub>2</sub>/g-C<sub>3</sub>N<sub>4</sub> materials was inspected by SEM, TEM, BET, and EDS, and the results showed that close interfacial connections between TiO<sub>2</sub> and g-C<sub>3</sub>N<sub>4</sub>, which are favorable for charge transfer between these two semiconductors, formed heterojunctions with suitable band structure which was contributed by the molten B<sub>2</sub>O<sub>3</sub>. Meanwhile, the molten B<sub>2</sub>O<sub>3</sub> effectively increased the specific surface area of TiO<sub>2</sub>/C<sub>3</sub>N<sub>4</sub> materials, thereby increasing the active sites and reducing the recombination of photogenerated electron–hole pairs and improving the photocatalytic degradation abilities of TiO<sub>2</sub> and g-C<sub>3</sub>N<sub>4</sub>. Elsewhere, the crystal structure analysis (XRD, XPS, FTIR) results indicated that the polar -B=O bond formed a new structure with TiO<sub>2</sub> and g-C<sub>3</sub>N<sub>4</sub>, which is not only beneficial for inhibiting the recombination of electron holes but also improving the photocatalytic activity. By removal experiment, the adsorption and degradation performances of B-TiO<sub>2</sub>/g-C<sub>3</sub>N<sub>4</sub> composite material were found to be 8.5 times and 3.4 times higher than that of g-C<sub>3</sub>N<sub>4</sub>. Above all, this study prepared a material for removing water pollutants with high efficiency and provides theoretical support and experimental basis for the research on the synergistic removal of pollutants by adsorption and photocatalysis.

**Keywords:** adsorption; degradation; B<sub>2</sub>O<sub>3</sub>; TiO<sub>2</sub>/C<sub>3</sub>N<sub>4</sub>; molten



**Citation:** Guo, X.; Rao, L.; Shi, Z. Preparation of High-Porosity B-TiO<sub>2</sub>/C<sub>3</sub>N<sub>4</sub> Composite Materials: Adsorption–Degradation Capacity and Photo-Regeneration Properties. *Int. J. Environ. Res. Public Health* **2022**, *19*, 8683. <https://doi.org/10.3390/ijerph19148683>

Academic Editors: Paul B. Tchounwou, Xin Zhao, Xun Wang and Zhiyuan Wang

Received: 24 June 2022

Accepted: 15 July 2022

Published: 17 July 2022

**Publisher's Note:** MDPI stays neutral with regard to jurisdictional claims in published maps and institutional affiliations.



**Copyright:** © 2022 by the authors. Licensee MDPI, Basel, Switzerland. This article is an open access article distributed under the terms and conditions of the Creative Commons Attribution (CC BY) license (<https://creativecommons.org/licenses/by/4.0/>).

## 1. Introduction

Photocatalysis is a technology that can use semiconductor materials to remove pollutants from the environment under different lighting conditions [1–3]. Most materials require ultraviolet conditions to produce redox effects. The visible part of sunlight irradiate that reaches the water surface only occupies 45%, while the ultraviolet part occupies less than 4% [4]. At the same time, water absorbs and reflects sunlight in different wavelengths, which seriously limits the removal efficiency of photocatalytic materials in a water environment [5–7].

g-C<sub>3</sub>N<sub>4</sub> is a good semiconductor material with application potential that is metal free and has visible light responsiveness [8–10]. However, researchers found that g-C<sub>3</sub>N<sub>4</sub> still has many disadvantages such as low utilization of visible light, poor photoelectric conversion efficiency, and low specific surface area [11]. Since Serpone et al. [12] first reported that a solid–solid heterojunction interface with good contact can be constructed from different coupled semiconductor materials to promote electron transfer between particles, more and more researchers have paid attention to different semiconductor materials. Among the many photocatalytic semiconductor materials, TiO<sub>2</sub> is widely used in sewage treatment [13], photocatalytic synthesis [14], and self-cleaning [15]. Due to its easy availability, low cost, stable chemical properties, corrosion resistance, non-toxicity, and strong oxidizing properties [16], its air purification [17] and antibacterial properties [18] have been extensively

studied. Therefore, using the advantages of  $\text{TiO}_2$  material properties to composite it with  $\text{g-C}_3\text{N}_4$  to become a more competitive material has attracted the attention of more and more researchers [19–21].

In the treatment of water environment pollution, the adsorption performance and visible light response ability of photocatalytic materials are two important factors that determine whether the photocatalytic technology can be effectively promoted [22,23]. The high-efficiency adsorption and enrichment ability of the material reduce the concentration of pollutants in water and provide a high-concentration contact environment that is conducive to the photocatalytic reaction for the material [24,25]. The melting characteristics of  $\text{B}_2\text{O}_3$ -modified  $\text{g-C}_3\text{N}_4$  are effective for improving its specific surface area and adsorption performance, but its response to visible light is limited, which affects the visible light photocatalytic activity [26].

Effectively improving the adsorption performance and visible light catalytic activity of materials at the same time is a key issue for researchers. Functional coupling through different materials is an idea to solve this problem. Here,  $\text{TiO}_2$  and  $\text{g-C}_3\text{N}_4$  were formed into a composite heterostructure to improve the photocatalytic oxidation ability of the material. Then, the melting characteristics of  $\text{B}_2\text{O}_3$  during the heating process were used as a “reaction environment regulator”, and  $\text{TiO}_2/\text{C}_3\text{N}_4$  was co-calcined to prepare a composite material. The results of the experiment showed that B element doped the composite-modified materials, and, finally, the adsorption behavior and visible light catalytic degradation ability of  $\text{B-TiO}_2/\text{C}_3\text{N}_4$  were analyzed by using MB and RhB organic pollutants. This method effectively increased the specific surface area of the material, increased the conjugated system, improved the adsorption capacity, and effectively improved the visible light catalytic effect of the material. This provides a technical idea for the promotion and application of a low-cost preparation of an efficient adsorption–degradation photocatalytic composite material.

## 2. Materials and Methods

### 2.1. Sample Preparation

- (1)  $\text{TiO}_2$ : 17 mL of butyl titanate (Aladdin, 99% pure) was placed into 55 mL of ethanol solution (Aladdin, 99.7% pure), then 4.5 mL of glacial acetic acid (Aladdin, 99% pure) was added. After mixing using a magnetic stirrer, the solution was recorded as A. We measured 27.6 mL of ethanol, added 0.9 mL of distilled water, and adjusted the pH to 4 with nitric acid (Sinopharm, 65–68% pure), and this solution was recorded as B after thorough mixing. The solutions A and B were stirred for 30 min respectively, the B solution was added dropwise to the A solution at a rate of 10 drops per minute, and the final obtained mixed solution was  $\text{TiO}_2$  sol. Then, the  $\text{TiO}_2$  sol was stirred at room temperature and placed in an oven to dry after gelation. Then, the dried xerogel was ground into powder and placed in a crucible with a lid to heat at a rate of  $5\text{ }^\circ\text{C}/\text{min}$  until  $550\text{ }^\circ\text{C}$  and was maintained at this temperature for 2 h. After the temperature in the muffle furnace (XS2–10, Li Chen, China) dropped to room temperature, the calcined material was ground into powder, and the obtained material was denoted as  $\text{TiO}_2$ .
- (2)  $\text{g-C}_3\text{N}_4$ : 10 g melamine (Aladdin, 99% pure) was placed into a 50 mL crucible and put into muffle furnace, and the heating rate was set to  $5\text{ }^\circ\text{C}/\text{min}$  until it reached the reaction temperature of  $550\text{ }^\circ\text{C}$ . Then, the reaction temperature was maintained for 2 h. After the material cooled to room temperature, we ground the calcined solid, and the obtained yellow powder was  $\text{g-C}_3\text{N}_4$ .
- (3)  $\text{TiO}_2/\text{C}_3\text{N}_4$  composite material: 1 g of melamine and 10 mL of  $\text{TiO}_2$  sol were weighed in a beaker, stirred, and mixed thoroughly and then the mixture was placed into an oven for drying after gelation. The dried composite precursor was placed in a crucible with a lid and calcined at  $550\text{ }^\circ\text{C}$  for 2 h. The obtained material was ground into powder after cooling to room temperature to obtain  $\text{TiO}_2/\text{C}_3\text{N}_4$  composite material.

- (4) B-C<sub>3</sub>N<sub>4</sub>: The B<sub>2</sub>O<sub>3</sub> (Aladdin, 99.9% pure) and g-C<sub>3</sub>N<sub>4</sub> were mixed and ground evenly. Then, the composite powder was placed into a ceramic crucible. After that, the samples were heated to 550 °C at a heating rate of 5 °C/min and maintained for 2 h. When the furnace was cooled to room temperature, the powders were washed with water and ethanol several times. For convenience of description, the composite material was abbreviated as B-C<sub>3</sub>N<sub>4</sub>.
- (5) B-TiO<sub>2</sub>/C<sub>3</sub>N<sub>4</sub>: The TiO<sub>2</sub>/C<sub>3</sub>N<sub>4</sub> material and B<sub>2</sub>O<sub>3</sub> were mixed and stirred in distilled water at a mass ratio of 1:1. After grinding evenly, we put it into an atmosphere furnace at 550 °C for 2 h. Then, the material was soaked and washed three times with ethanol and distilled water, respectively. The sample was denoted as B-TiO<sub>2</sub>/C<sub>3</sub>N<sub>4</sub>. For comparison, another ternary composite material, B<sub>2</sub>-C<sub>3</sub>N<sub>4</sub>/TiO<sub>2</sub>, was prepared: 1 g of B-C<sub>3</sub>N<sub>4</sub> and 10 mL of TiO<sub>2</sub> sol were weighed with the same method.

## 2.2. Characterization

The structural analysis of the samples was carried out by X-ray diffraction (XRD, Rigaku Ultima III, Tokyo, Japan) and was recorded in the 2θ range of 5–80° with a scan rate of 0.02°/0.4 s using a Bruker AXSD8 system (Bruker, Billerica, MA, USA) equipped with a Cu Kα radiation source (λ = 0.15406 Å, in which the X-ray tube was operated at 40 kV and 40 mA). UV–Vis diffuse reflectance spectra (DRS) were obtained on a UV–visible (UV–Vis) spectrophotometer (PerkinElmer, Waltham, MA, USA) with BaSO<sub>4</sub> as the reference. The sample morphology of the different composite materials was examined using a scanning electron microscope (SEM, Hitachi, Tokyo, Japan) and a transmission electron microscope (TEM, JEM-2100, JEOL, Tokyo, Japan). X-ray photoelectron spectroscopy (XPS) measurements were performed on a Thermo Scientific ESCALAB 250 instrument (Thermo Fisher Scientific, Waltham, MA, USA) with an Al Kα source. Low-temperature N<sub>2</sub> adsorption/desorption measurements (Brunauer–Emmett–Teller (BET) method) were carried out using a Micromeritics ASAP 2020 system (Micromeritics, Norcross, GA, USA) at –196 °C following degassing of all samples at 120 °C for 2 h.

## 2.3. Adsorption and Photocatalytic Degradation of Organic Pollution

In order to evaluate whether composite materials have a better effect on the removal of pollutants, TiO<sub>2</sub>, g-C<sub>3</sub>N<sub>4</sub>, B-TiO<sub>2</sub>, B-C<sub>3</sub>N<sub>4</sub>, TiO<sub>2</sub>/C<sub>3</sub>N<sub>4</sub>, B-TiO<sub>2</sub>/C<sub>3</sub>N<sub>4</sub>, and B<sub>2</sub>-C<sub>3</sub>N<sub>4</sub>/TiO<sub>2</sub> were weighed in the removal experimental. A 30 mg amount of each of material was added to the MB solution with a volume of 100 mL and a concentration of 20 mg/L. Under the condition of magnetic stirring, the photocatalytic efficiency was measured after 30 min of dark reaction adsorption experiment. A 1.5 mL amount of solution was taken out for measurement each time, and the removal rate of pollutants was determined by the following formula:

$$R_t = \frac{C_0 - C_t}{C_0} \times 100\% \quad (1)$$

where  $R_t$  is the removal rate at time  $t$  after commencing the adsorption and photocatalytic degradation process, and  $C_0$  and  $C_t$  are initial concentration and concentration at time  $t$ , respectively.

$$Q_e = \frac{C_0 - C_e}{m} V \quad (2)$$

where  $Q_e$  is the adsorbed quantity of samples at the equilibrium moment of adsorption and desorption.  $C_0$ ,  $C_e$ ,  $V$ , and  $m$  are the initial concentration, concentration at time  $t$ , initial volume of MB, and quantity of adsorbent, respectively.

## 2.4. Kinetics and Adsorption Isotherm Model

The adsorption behaviors were fitted to the materials by pseudo-first-order kinetic and pseudo-second-order kinetic models, respectively. Two kinetic linear models are shown below [27]:

Pseudo-first-order kinetic model:

$$\ln(Q_e - Q_t) = \ln Q_e - k_1 t \quad (3)$$

Pseudo-second-order kinetic model:

$$\frac{t}{Q_t} = \frac{1}{k_2 Q_e^2} + \frac{t}{Q_e} \quad (4)$$

where  $Q_t$  and  $Q_e$  in the formula are the adsorption amount of the sample at time  $t$  and equilibrium, respectively.  $k_1$  and  $k_2$  are pseudo-first-order kinetic constants and pseudo-second-order kinetic constants, respectively.

Langmuir and Freundlich are the two most common adsorption isotherm models. The Langmuir model assumes that the surface of the adsorbate is uniform and the adsorption capacity is the same everywhere, and it only occurs on the outer surface of the adsorbent; this is monolayer adsorption. The Freundlich adsorption equation can be applied to both monolayer adsorption and adsorption behavior on uneven surfaces. Freundlich, as an empirical adsorption isotherm for non-uniform surfaces, is more applicable to low-concentration adsorption and can interpret experimental results over a wider concentration range. Therefore, in this experiment, the experimental results are fitted by these two adsorption isotherm models, and the formulas are as follows [28]:

Langmuir:

$$\frac{C_e}{Q_e} = \frac{1}{Q_m K_L} + \frac{C_e}{Q_m} \quad (5)$$

Freundlich:

$$\ln Q_e = \frac{1}{n} \ln C_e + \ln K_F \quad (6)$$

where  $Q_e$  and  $Q_m$  represent the adsorption capacity and the maximum adsorption capacity, respectively;  $C_e$  is the concentration of pollutants in the solution at adsorption equilibrium;  $K_L$  is the Langmuir adsorption equilibrium constant; and  $K_F$  is the Freundlich constants with the affinity coefficient.

### 3. Result and Discussion

#### 3.1. Performance Testing

In order to study the physical and chemical properties of the materials, the materials were screened by the adsorption catalytic performance of removing pollutant MB (Figure S1). It can be clearly seen from the figure that the adsorption–catalytic efficiency of several different materials for removing MB under the dark reaction and visible light conditions was  $B\text{-TiO}_2/\text{C}_3\text{N}_4 > B\text{-C}_3\text{N}_4 > B2\text{-C}_3\text{N}_4/\text{TiO}_2 > \text{TiO}_2/\text{C}_3\text{N}_4 > B\text{-TiO}_2 > g\text{-C}_3\text{N}_4 > \text{TiO}_2$ . Among them, the adsorption and removal rate of MB on  $B\text{-TiO}_2/\text{C}_3\text{N}_4$  in the dark reaction process reached 73.8%, while that of  $B2\text{-C}_3\text{N}_4/\text{TiO}_2$  was only 17.8%. Then, under the visible light condition for 2 h, the removal rate of MB by  $B\text{-TiO}_2/\text{C}_3\text{N}_4$  reached 97.3%, while that of  $B2\text{-C}_3\text{N}_4/\text{TiO}_2$  only reached 66.5%. Therefore, according to the preliminary experimental results, the  $B\text{-TiO}_2/\text{C}_3\text{N}_4$  material was selected as the composite photocatalyst with the highest removal efficiency for follow-up research.

The mixing ratio and calcination temperature of the composites are both important factors affecting the performance of the composite materials. Therefore, in order to further analyze the performance of the composite material, this experiment first selected  $B_2O_3$  and  $\text{TiO}_2/\text{C}_3\text{N}_4$  with different mass ratios to be mixed and calcined at 550 °C and then selected the material with the best pollutant removal effect for subsequent experiments.

According to the amount of doping of  $B_2O_3$ , the composite materials were marked as  $B\text{-TiO}_2/\text{C}_3\text{N}_4\text{-}x$  ( $x = 1, 2, 3, 4, 5$ ). The removal efficiencies are shown in Figure S2. The removal rates of  $B\text{-TiO}_2/\text{C}_3\text{N}_4\text{-}1$ ,  $B\text{-TiO}_2/\text{C}_3\text{N}_4\text{-}2$ , and  $B\text{-TiO}_2/\text{C}_3\text{N}_4\text{-}3$  were 69.3%, 83.2%, and 73.4%, respectively, while the removal rates of  $B\text{-TiO}_2/\text{C}_3\text{N}_4\text{-}4$  and  $B\text{-TiO}_2/\text{C}_3\text{N}_4\text{-}5$  were only 50.9% and 23.9%.

Therefore, according to the above experimental results, B-TiO<sub>2</sub>/C<sub>3</sub>N<sub>4</sub>-2 had the best effect and was selected as the follow-up research material. A 2 g amount of B<sub>2</sub>O<sub>3</sub> and 1 g of TiO<sub>2</sub>/C<sub>3</sub>N<sub>4</sub> material were mixed uniformly, and the mixture temperature was heated at a rate of 5 °C/min for 2 h at different temperatures. The set target temperatures were 350 °C, 450 °C, 550 °C, 650 °C, and 750 °C. For convenience of description, B-TiO<sub>2</sub>/C<sub>3</sub>N<sub>4</sub> prepared at different calcination temperatures was named after its temperature (350 °C, 450 °C, 550 °C, 650 °C, and 750 °C).

### 3.2. Characterization and Analysis of B-TiO<sub>2</sub>/C<sub>3</sub>N<sub>4</sub> Composites

The morphology of B-TiO<sub>2</sub>/C<sub>3</sub>N<sub>4</sub> composites prepared under different calcination conditions at different temperatures are shown in Figure 1. It can be seen from Figure 1a that at 350 °C the surface of the structure was relatively smooth, which may have been due to molten B<sub>2</sub>O<sub>3</sub> wrapping the base material. Figure 1b shows the surface layer of the calcined material at 450 °C was still partially covered, but a large number of loose structures also appeared. This may have been due to the increase in the calcination temperature, and the disorder degree increased due to the B<sub>2</sub>O<sub>3</sub> entering the molten state, which contains polar -B=O groups. As seen in Figure 1c, many loose pores appeared on the surface of the composite under the 550 °C calcination condition. As the temperature continued to increase, the main structure of the g-C<sub>3</sub>N<sub>4</sub> material began to decompose when the temperature was above 600 °C, and the pulverization of the g-C<sub>3</sub>N<sub>4</sub> structure can be clearly seen in Figure 1d. At 750 °C, g-C<sub>3</sub>N<sub>4</sub> was decomposed into nitrogen and nitrile-based fragments, and TiO<sub>2</sub> was gradually transformed from anatase to rutile; so, the layered structure of g-C<sub>3</sub>N<sub>4</sub> cannot be observed in Figure 1e, while some agglomerates of particles can be seen.

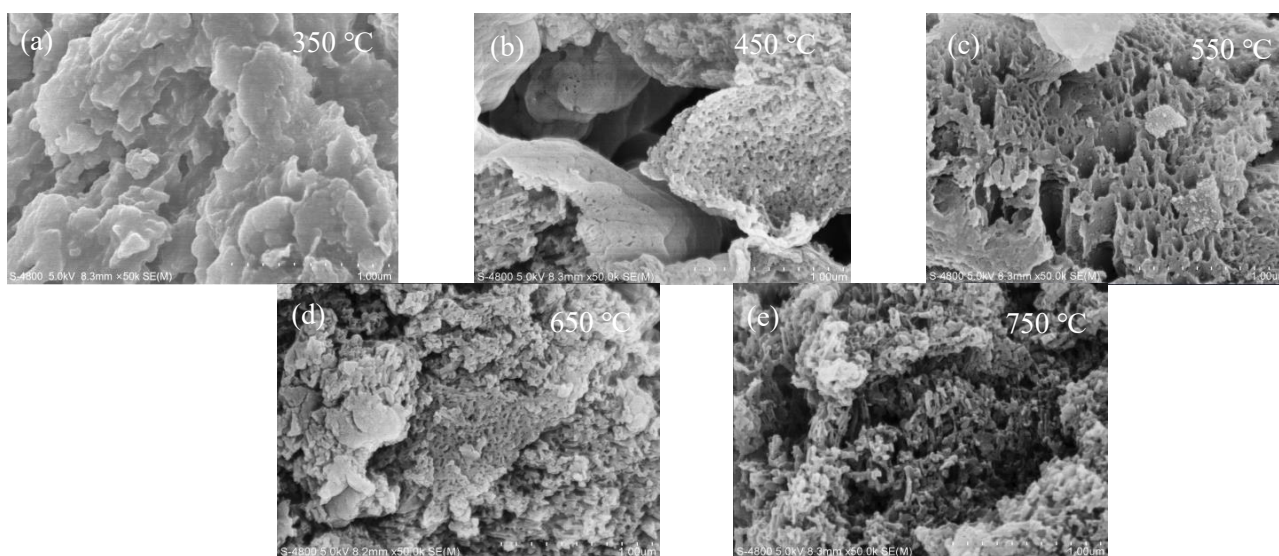


**Figure 1.** SEM of B-TiO<sub>2</sub>/C<sub>3</sub>N<sub>4</sub> under different calcination conditions: (a) 350 °C; (b) 450 °C; (c) 550 °C; (d) 650 °C; (e) 750 °C.

The specific surface area and porosity of materials are crucial factors affecting the adsorption and photocatalytic reactions. As shown in Figure S3, the representative N<sub>2</sub> adsorption–desorption isotherms of composite materials were of type IV [29]. According to the classification of IUPAC, the adsorption and desorption curve hysteresis loop types of the prepared B-TiO<sub>2</sub>/C<sub>3</sub>N<sub>4</sub> materials belonged to the “H3” hysteresis loop (0.5 < P/P<sub>0</sub> < 0.98:550 °C, 650 °C, 750 °C; 0.75 < P/P<sub>0</sub> < 0.97:350 °C, 450 °C). The low-temperature calcination shown for loops located at high P/P<sub>0</sub> was caused by the aggregation of the 2D lamellar structure of g-C<sub>3</sub>N<sub>4</sub>. By contrast, the high temperature and B<sub>2</sub>O<sub>3</sub> as a medium effectively resulted in more holes on the surface of g-C<sub>3</sub>N<sub>4</sub>. In Table 1, details regarding the specific surface areas, average pore diameters, and pore volumes of various materials are summarized. Among the temperature series, 550 °C showed the highest specific surface areas, average

pore diameters, and pore volumes. This is because, at the calcination temperature of 550 °C, the molten B<sub>2</sub>O<sub>3</sub> could fully contact the TiO<sub>2</sub>/C<sub>3</sub>N<sub>4</sub> composite as a reaction environment modifier. The lamellar structure of g-C<sub>3</sub>N<sub>4</sub> was exfoliated in the molten environment while the pore structure was formed during the cooling process, so the specific surface area was significantly increased.

**Table 1.** BET surface area, average pore size, and pore volume of B-TiO<sub>2</sub>/C<sub>3</sub>N<sub>4</sub> material at different temperatures.

Sample	350 °C	450 °C	550 °C	650 °C	750 °C
BET (m <sup>2</sup> /g)	13.381	13.472	58.654	34.622	25.795
Average pore size (nm)	6.311	7.809	6.960	12.733	14.263
Average pore volume (cm <sup>3</sup> /g)	0.090	0.073	0.130	0.162	0.103

The surface morphologies and microstructure of B-TiO<sub>2</sub>/C<sub>3</sub>N<sub>4</sub> (550 °C) composite material are shown in Figure 2. From Figure 2a,b, it can be clearly observed that there were a lot of loose macropores and particle agglomeration on the surface of the g-C<sub>3</sub>N<sub>4</sub>-based material. In order to better analyze the morphological characteristics of the material, the high-resolution transmission electron microscope (HR-TEM) pattern was used for analysis. In Figure 2c, it can be seen that there were a lot of loose pores on the surface of the g-C<sub>3</sub>N<sub>4</sub>. Otherwise, a large number of granular material lattice fringes appeared on the g-C<sub>3</sub>N<sub>4</sub> lamellar structure. The lattice spacing embedded particles were measured to be ~0.35 nm (Figure 2d), which is similar to the TiO<sub>2</sub> (101) crystal plane structure [30]. Through the analysis of specific surface area and the characterization of SEM and TEM, it was found that TiO<sub>2</sub> grew uniformly on the surface of the g-C<sub>3</sub>N<sub>4</sub> layered structure, and the modification of the TiO<sub>2</sub>/C<sub>3</sub>N<sub>4</sub> composite structure by B<sub>2</sub>O<sub>3</sub> produced a large number of loose pores on the g-C<sub>3</sub>N<sub>4</sub> layered structure. Such a modification method not only improved the specific surface area of the material, but also preserved the composite structure of TiO<sub>2</sub>/C<sub>3</sub>N<sub>4</sub>, which is more conducive to the charge transfer of photogenerated carriers between composite semiconductor materials and improves the photocatalytic activity of the material.

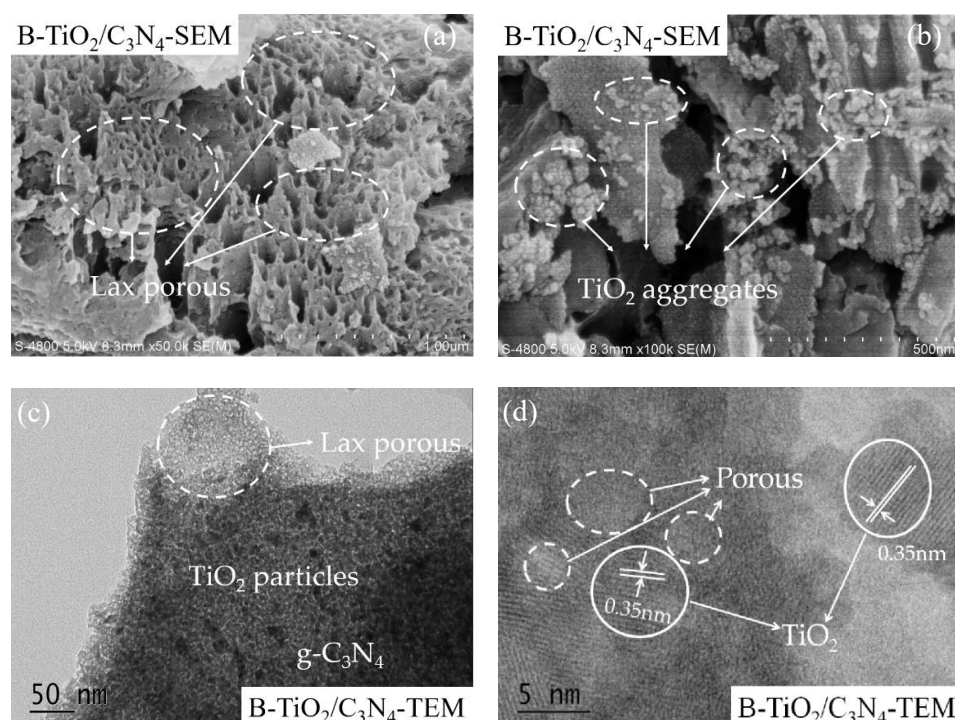


**Figure 2.** SEM (a,b) and TEM (c,d) spectra of B-TiO<sub>2</sub>/C<sub>3</sub>N<sub>4</sub> (550 °C) composite materials.

The XRD pattern of materials was recorded and is shown in Figure S4. It can be seen that  $B_2O_3$  showed two obvious, characteristic peaks at  $14.6^\circ$  and  $27.9^\circ$  [31]. The composites prepared at  $350^\circ C$  and  $450^\circ C$  had only two obvious characteristic peaks of  $B_2O_3$  but no characteristic peaks of  $TiO_2$  and  $g-C_3N_4$  [32]. This may have been because the surface of the  $TiO_2/C_3N_4$  material was coated by  $B_2O_3$  in the molten state at  $350^\circ C$  and  $450^\circ C$ , which is basically consistent with the SEM characterization shown in Figure 1. At the same time, due to the large amount of  $B_2O_3$  added, there was no peak position of  $g-C_3N_4$  and  $TiO_2$  but only the characteristic peak of  $B_2O_3$ . At  $550^\circ C$ , the two characteristic peaks of  $B_2O_3$  disappeared in the XRD pattern, and the anatase ( $25.3^\circ$ ) and rutile ( $27.4^\circ$ ) diffraction peaks of  $TiO_2$  appeared. It was caused by the entry of polar  $-B=O$  into the  $TiO_2/C_3N_4$ . When the temperature rose to  $650^\circ C$ , several characteristic peaks ( $27.4^\circ$ ,  $41.3^\circ$ , etc.) of the rutile phase of  $TiO_2$  became more and more obvious, which indicated that the crystal structure of  $TiO_2$  gradually changed from anatase to rutile with the increase in temperature. It can be seen from XRD analysis that when the temperature gradually increased, the degree of disorder gradually increased, and a polar  $-B=O$  bond was formed to form a new structure with  $TiO_2$  or  $g-C_3N_4$  [33].

The Fourier-transform infrared spectroscopy of composite materials is shown in Figure S5. In this figure, it can be seen that the peak at  $550^\circ C$  was the smallest, which was the  $Ti-O$  bond expansion joint and  $Ti$  stretching vibration of the  $-O-Ti$  bond. Compared with the  $B-TiO_2/C_3N_4$  composites at different calcination temperatures ( $350^\circ C$ ,  $450^\circ C$ ,  $550^\circ C$ ,  $650^\circ C$ , and  $750^\circ C$ ), the obvious peaks appeared at  $810\text{ cm}^{-1}$  and  $1200\text{--}1600\text{ cm}^{-1}$ . The characteristic peak at  $810\text{ cm}^{-1}$  was the stretching vibration of the triazine ring structure in  $g-C_3N_4$ , while the broad peak spectrum at  $1200\text{--}1600\text{ cm}^{-1}$  was caused by the stretching vibration of  $C=N$ . Otherwise, the obvious differences of all composite materials were mainly due to the incomplete transformation of  $B_2O_3$  from solid to molten state. At low temperatures, the peaks were not obvious, which was caused by molten  $B_2O_3$  coating on the surface of composite material, resulting in limited exposure of the surface structure of the  $B-TiO_2/C_3N_4$  composite. In addition, the absorption peaks of  $B-TiO_2/C_3N_4$  composites at  $3000\text{--}3300\text{ cm}^{-1}$  were mainly the stretching vibration of the amino group ( $-NH_2$ ). Meanwhile, the two peaks at  $2260\text{ cm}^{-1}$  and  $2350\text{ cm}^{-1}$  were the  $C=O$  stretching vibration of  $CO_2$  in the atmosphere [34].

Figure S6 shows the XPS spectra of several elements of  $B-TiO_2/C_3N_4$ : B1s, N1s, C1s, Ti2s and O1s. B1s shows three binding energies at 190.4 eV, 192.7 eV, and 193.5 eV, of which 192.7 eV belonged to the  $B-O$  bond, 190.4 eV was the binding energy of the  $B-N$  bond, and 193.5 eV may have been  $O-B$  formed by B entering the  $TiO_2$  crystal structure— $Ti$  or  $TiB_2$  bond [35]. This indicates that B element entered into the structures of  $TiO_2$  and  $g-C_3N_4$ . C1s showed three main binding energies, of which 284.8 eV was the typical  $sp^2$  hybridization of the graphite phase ( $C=C$  bond peak position), and 288.7 eV corresponded to the  $C-N-C$  bond in the structure. In addition, 286.5 eV corresponded to the exocyclic  $C-O$  of carbon-nitrogen polymer materials [36]. Figure S6c shows the N1s binding energy peaks at 397.3 eV, 398.2 eV, and 401.9 eV. Among them, 398.2 eV was attributed to the  $sp^2$  hybridization ( $C-N=C$ ) of the N triazine ring structure, while the peak at 401.9 eV corresponded to the bridged N atom ( $N-(C)^3$ ) [37], and the peak at 397.3 eV corresponded to  $N-B$  [38]. In addition, the characteristic peaks in the N spectrum were slightly shifted, possibly due to the increased delocalization between the large  $\pi$  bonds in the carbon nitride structure due to the doping of B element [29]. The two peaks of 458.7 eV and 464.8 eV in the binding energy of Ti 2s were the electron binding energies of  $Ti^{4+} 2p^{3/2}$  and  $2p^{1/2}$  in  $TiO_2$ , respectively. The strong peak at 530.1 eV in the O1s spectrum was the  $O-Ti$  bond in  $TiO_2$ , while 531.0 eV and 532.7 eV were the surface-adsorbed water molecules,  $H_2O$  and surface hydroxyl groups ( $-OH$ ), respectively [39].

Figure S7 shows the UV-Vis diffuse reflectance absorption spectra of the composite material ( $350^\circ C$ ,  $450^\circ C$ ,  $550^\circ C$ ,  $650^\circ C$ ,  $750^\circ C$ ). It can be seen from the figure that under different temperature conditions, the UV-visible light absorption properties of the composites were different. The  $B-TiO_2/C_3N_4$  prepared at the three temperatures of

350 °C, 450 °C, and 550 °C had better visible light absorption ability in both the ultraviolet and visible light regions, and the effect of 550 °C was the best. This result was caused by B element entering into the TiO<sub>2</sub> lattice and g-C<sub>3</sub>N<sub>4</sub> structure. According to the low electronegativity of B element, it can be inferred that the 2p orbital of B may be different from the 2p orbital of O. Hybridization was generated, thus, enabling enhanced visible light absorption [40]. Otherwise, the 650 °C and 750 °C had high light absorption capacity in the ultraviolet regions of 200–350 nm and 200–400 nm, respectively. The light absorption ability of the visible light region greater than 400 nm was weak. This may have been due to the gradual decomposition of the g-C<sub>3</sub>N<sub>4</sub> structure in the composite material with the increase in temperature, resulting in a decrease in the visible light absorption capacity of the material. At the same time, although the temperature increased, it could also have caused the transformation of the TiO<sub>2</sub> crystal phase, while the mixed-phase TiO<sub>2</sub> had visible light absorption ability, but the effect was not obvious. Therefore, according to the UV–Vis diffuse reflectance spectrum analysis, it is shown that the B-TiO<sub>2</sub>/C<sub>3</sub>N<sub>4</sub> composites prepared at 550 °C had good light absorption ability.

Based on the above characterization analysis description, we can roughly infer the preparation process of composite materials. The TiO<sub>2</sub>/C<sub>3</sub>N<sub>4</sub> material was exfoliated by using the molten reaction environment provided by B<sub>2</sub>O<sub>3</sub> during the heating process. At the same time, the gas was decomposed by the trace amount of g-C<sub>3</sub>N<sub>4</sub>, thereby forming a large number of loose pore structures. With the increase in calcination temperature, the generated polar -B=O bond replaced the H atom of the amino group on carbon nitride melon and formed an O–B–Ti or TiB<sub>2</sub> structure, thereby finally forming a structurally stable B-TiO<sub>2</sub>/C<sub>3</sub>N<sub>4</sub> material. The specific reaction process inference diagram is shown in Figure S8.

### 3.3. Photocatalytic Efficiencies

Figure 3 shows the dark adsorption and light-driven photocatalytic degradation ability of MB (a) and RhB (b) of B-TiO<sub>2</sub>/C<sub>3</sub>N<sub>4</sub> composite materials (350 °C, 450 °C, 550 °C, 650 °C, and 750 °C). The specific experimental process was as follows: 30 mg of B-TiO<sub>2</sub>/C<sub>3</sub>N<sub>4</sub> composite was added into 100 mL of MB solution with a concentration of 20 mg/L and 10 mg/L of RhB solution, respectively. A half-hour dark reaction time was set in the experiment and then the photocatalytic degradation experiment was carried out. The removal ability of RhB and MB was analyzed by catalytically degrading RhB and MB under the irradiation of a xenon light source with a wavelength greater than 400 nm.

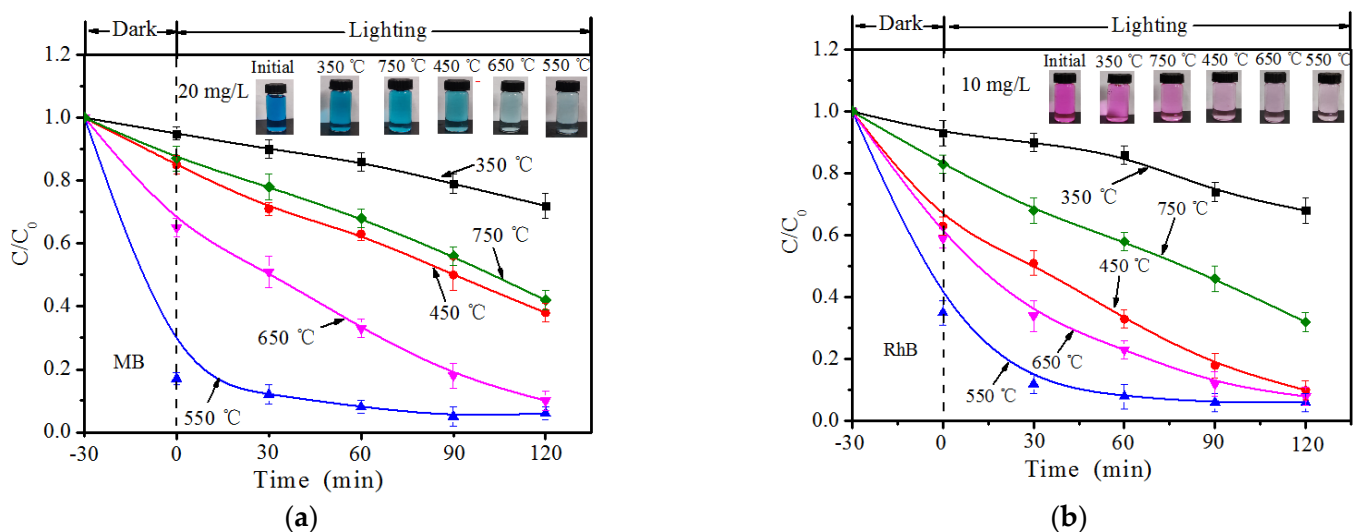


**Figure 3.** The adsorption–photocatalytic degradation curves of MB (a) and RhB (b) over B-TiO<sub>2</sub>/C<sub>3</sub>N<sub>4</sub>.

The calculation of the removal efficiency of each pollutant by several catalyst materials was calculated by Formula (1). The experimental results of the dark reaction and the light

reaction are shown in Figure 4a,b. The two figures show the adsorption–degradation curves of MB (20 mg/L) and RhB (10 mg/L) by the B-TiO<sub>2</sub>/C<sub>3</sub>N<sub>4</sub> composite, respectively. The relationship among the adsorption–degradation efficiencies can be clearly seen from the figure: 550 °C > 650 °C > 450 °C > 750 °C > 350 °C. The B-TiO<sub>2</sub>/C<sub>3</sub>N<sub>4</sub> prepared at the 550 °C calcination temperature had the best adsorption effect on the two dyes in the dark reaction adsorption process and the best removal efficiency (83.4% (MB), 64.1% (RhB)). At this temperature, B<sub>2</sub>O<sub>3</sub> may undergo a complete molten state process, and become a good molten state reaction environment to fully contact with TiO<sub>2</sub>/C<sub>3</sub>N<sub>4</sub>. Therefore, the prepared B-TiO<sub>2</sub>/C<sub>3</sub>N<sub>4</sub> had a larger specific surface area, exposing more adsorption sites and a reaction active site. Therefore, the doping of B element is beneficial to improve photocatalytic activity. When the temperature continued to rise above 600 °C, the g-C<sub>3</sub>N<sub>4</sub> material began to decompose gradually, and the TiO<sub>2</sub> gradually transformed from anatase type to rutile phase with lower photocatalytic reaction activity, so the photocatalytic reaction efficiency decreased gradually.

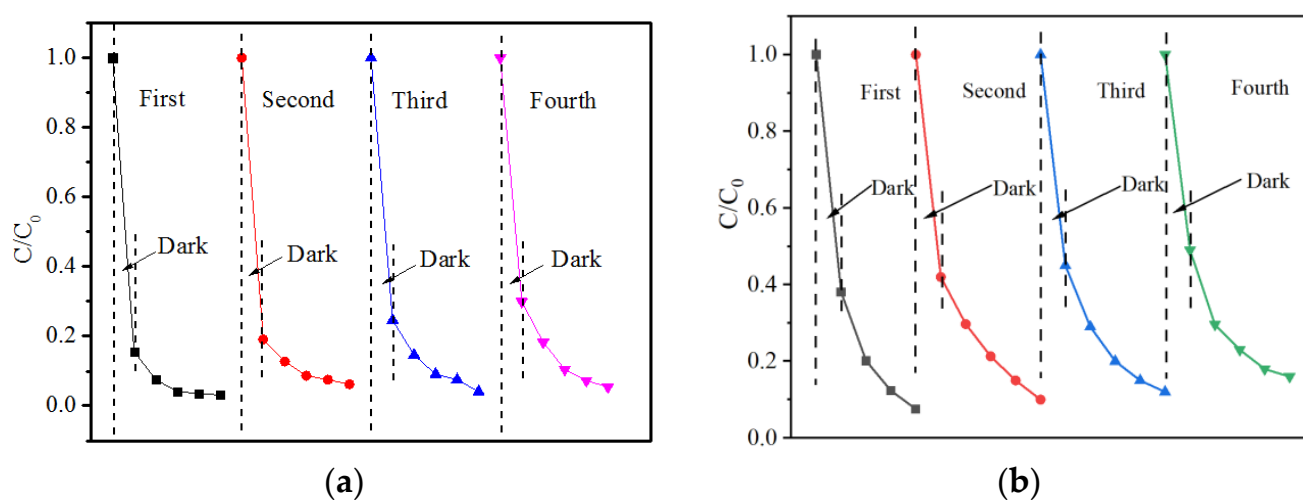


**Figure 4.** Cycling experiments of B-TiO<sub>2</sub>/C<sub>3</sub>N<sub>4</sub> for the adsorption–photocatalytic degradation of MB (a) and RhB (b).

Meanwhile, multiple cycle experiments were carried out with MB and RhB. It can be seen from Figure 4 that after four cycles of repeated tests, the adsorption and removal rate of B-TiO<sub>2</sub>/C<sub>3</sub>N<sub>4</sub> to 20 mg/L organic solution decreased from 83.4% to 70.1% (MB) and from 64.1% to 51.2% (RhB). The results showed that the adsorption effect of the material on MB and RhB was weakened gradually. This may have been because the pores on the surface of the material were damaged during the experiment. Meanwhile, the active sites were reduced due to the coverage of undegraded pollutants adsorbed on the surface of the material, resulting in a decrease in the adsorption and catalytic efficiency of the material after multiple experiments. Although the adsorption capacity of the material for the two pollutants was gradually weakened, the removal rate remained at around 95% (MB) and 80% (RhB) within two hours. This result shows that the B-TiO<sub>2</sub>/C<sub>3</sub>N<sub>4</sub> composite material had better stability and repeatability.

The TOC in the photocatalytic degradation system reflected the mineralization degree of organic pollutants. The results of the TOC are shown in Figure S9. The adsorption process effectively reduced the value. With the progress of visible light, the TOC value experienced small decreases with the prolongation of the lighting time. This is because, during the degradation process, the pollutant molecules were decomposed from macromolecules to small molecules containing organic carbon, and the pollutants adsorbed on the surface of the material were also desorbed. The resorption–degradation process resulted in insignificant changes in the organic carbon content in the solution [41,42].

### 3.4. Adsorption Property

To demonstrate the adsorption property of B-TiO<sub>2</sub>/C<sub>3</sub>N<sub>4</sub> (550 °C) composite materials, adsorption and removal rates of RhB and MB were chosen as the contaminant. The adsorption efficiency plays an important role in the rapid removal of pollutants.

The kinetic curve of adsorption of MB and RhB on B-TiO<sub>2</sub>/C<sub>3</sub>N<sub>4</sub> is shown in Figure 5. From this figure, it can be seen that B-TiO<sub>2</sub>/C<sub>3</sub>N<sub>4</sub> reached the adsorption equilibrium for the two pollutants within 30 min; the adsorption capacity of MB reached 56.25 mg/g; and the adsorption capacity of RhB reached 18.94 mg/g. Compared with other materials (as shown in Figure S1), the improvement of adsorption efficiency was due to the increase in specific surface area and the increase in adsorption sites, and the doping of B element in g-C<sub>3</sub>N<sub>4</sub> expanded the large,  $\pi$ -bonded conjugated system, which was more conducive to the adsorption of MB [9].

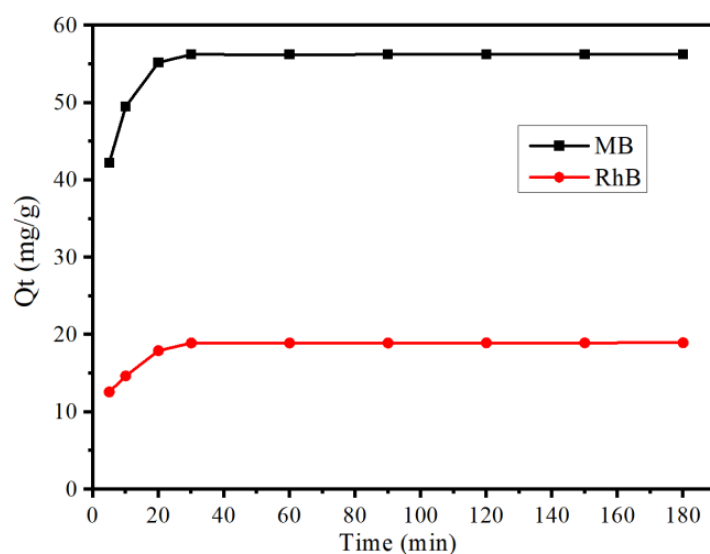


**Figure 5.** Adsorption kinetics curves of B-TiO<sub>2</sub>/C<sub>4</sub> on MB and RhB.

The pseudo-first-order kinetic and pseudo-second-order kinetic models were fitted to the adsorption amounts of MB and RhB, respectively. The results are shown in Figure 6. The fitted correlation coefficients were: MB:  $R_1^2 = 0.5017$  (a),  $R_2^2 = 0.9964$  (b); RhB:  $R_1^2 = 0.6872$  (c),  $R_2^2 = 0.9998$  (d). According to the correlation coefficients fitted to the two pollutants, it can be seen that the pseudo-second-order kinetic model better fitted the adsorption behavior of B-TiO<sub>2</sub>/C<sub>3</sub>N<sub>4</sub>.

Figure 7 shows the fitting of the Langmuir and Freundlich adsorption isotherm models for the adsorption of MB (a) (b) and RhB (c) (d) on B-TiO<sub>2</sub>/C<sub>3</sub>N<sub>4</sub>, respectively. By comparing the correlation coefficients obtained by calculation, it was found that for the MB adsorption isotherm model,  $R_L^2 = 0.9946$  was higher than that of the Freundlich model ( $R_F^2 = 0.6883$ ), while the simulated adsorption isotherm model for RhB had the same or similar results ( $R_L^2: 0.9993 > R_F^2: 0.7395$ ). This result showed that the adsorption of MB and RhB by B-TiO<sub>2</sub>/C<sub>3</sub>N<sub>4</sub> was monolayer adsorption, and the adsorption was more favorable with the increase in pollutant concentration. Therefore, the adsorption of these two pollutants by B-TiO<sub>2</sub>/C<sub>3</sub>N<sub>4</sub> was more inclined to the Langmuir adsorption isotherm model.

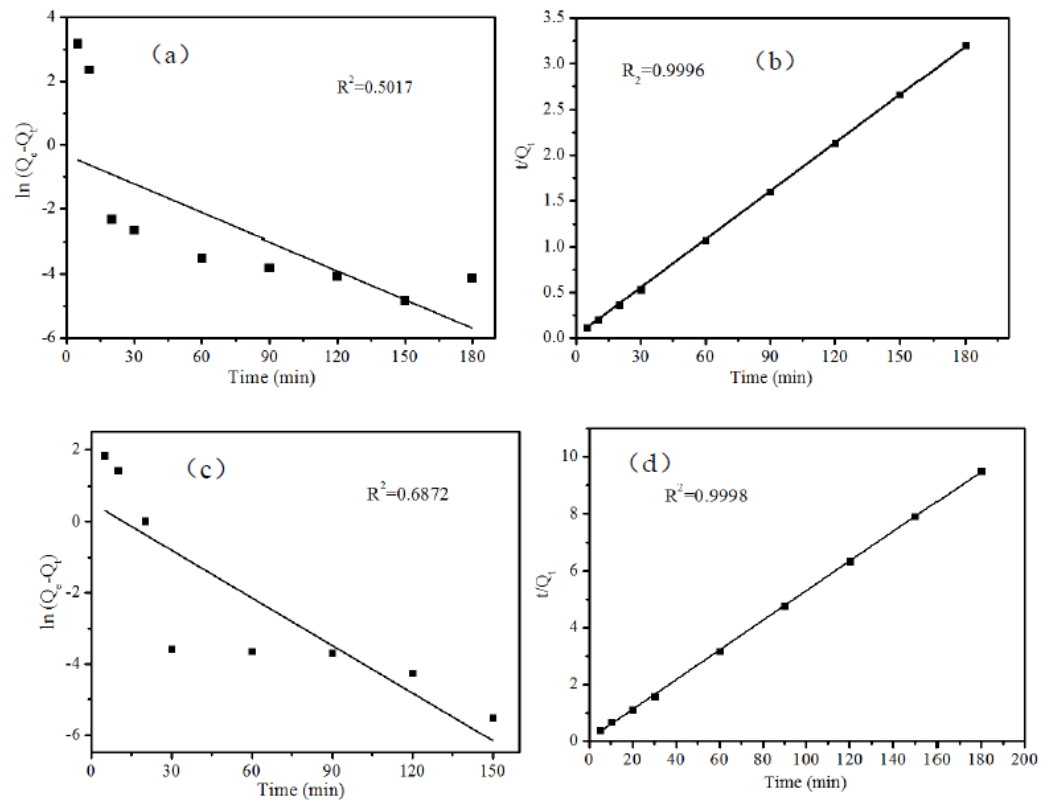


**Figure 6.** (a) Plots of the pseudo-first-order model (MB); (b) Plots of the pseudo-second-order model (MB); (c) Plots of the pseudo-first-order model (RhB); (d) Plots of the pseudo-second-order model (RhB).

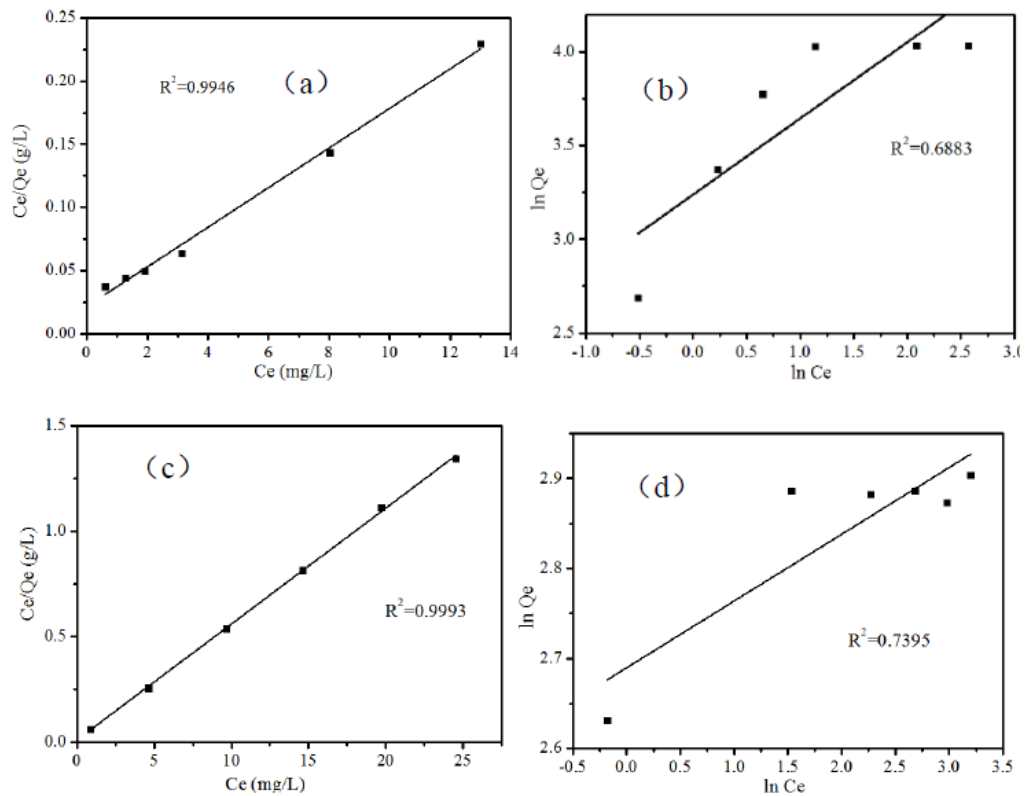


**Figure 7.** The linearized of Langmuir adsorption isotherm (a) MB (c) RhB and Freundlich adsorption isotherm (b) MB (d) RhB adsorption by B-TiO<sub>2</sub>/C<sub>3</sub>N<sub>4</sub>.

### 3.5. Analysis of Photocatalytic Mechanism

Based on the above experimental results, MB was selected as the target pollutant with the best removal effect, and the main substances involved in the photocatalytic reaction were determined by the free radical capture experiment. The experimental results are shown in Figure 8. The addition of EDTA-2Na had less of an effect on the degradation effect of MB, which indicates that the role of holes is less important in the catalytic reaction. After the addition of p-benzoquinone, the degradation of MB was inhibited, indicating that superoxide radical ( $\cdot\text{O}_2^-$ ) is an important free radical involved in the photodegradation process. After the addition of tert-Butanol, the degradation of MB was also inhibited to a certain extent, so it can be concluded that hydroxyl radicals ( $\cdot\text{OH}$ ) are also involved in the photocatalytic oxidation process. The above research results show that  $\cdot\text{O}_2^-$  and  $\cdot\text{OH}$  radicals were the active groups that mainly participated in the reaction during the degradation of MB by B-TiO<sub>2</sub>/C<sub>3</sub>N<sub>4</sub>.

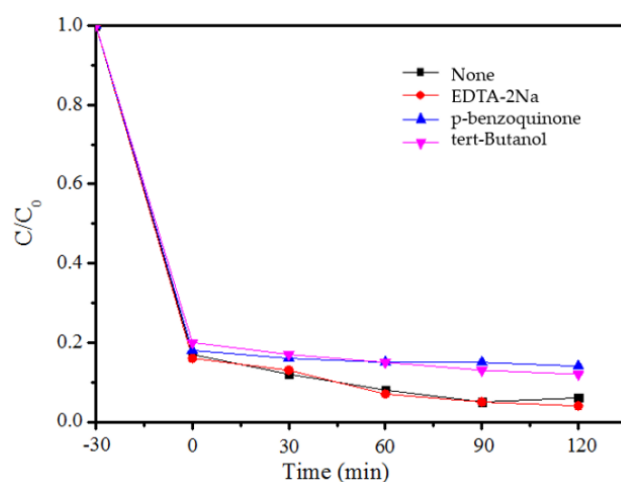


**Figure 8.** The capture experiments of MB by B-TiO<sub>2</sub>/C<sub>3</sub>N<sub>4</sub>.

Through mechanism analysis, it was found that  $\cdot\text{O}_2^-$  and  $\cdot\text{OH}$  were the main active groups involved in the photocatalytic reaction. Therefore, DMPO ESR was used to detect the  $\cdot\text{O}_2^-$  and  $\cdot\text{OH}$  produced by B-TiO<sub>2</sub>/C<sub>3</sub>N<sub>4</sub> material under visible light above 400 nm. In addition, a comprehensive comparative analysis was conducted with other materials. It can be clearly seen from Figure 9a that after 10 min of light source irradiation, the order of  $\cdot\text{O}_2^-$  ESR signal intensity was B-TiO<sub>2</sub>/C<sub>3</sub>N<sub>4</sub> > TiO<sub>2</sub>/C<sub>3</sub>N<sub>4</sub> > g-C<sub>3</sub>N<sub>4</sub> > B-C<sub>3</sub>N<sub>4</sub> > B-TiO<sub>2</sub> > TiO<sub>2</sub>. The signal peak generated by B-TiO<sub>2</sub>/C<sub>3</sub>N<sub>4</sub> was slightly higher than that of TiO<sub>2</sub>/C<sub>3</sub>N<sub>4</sub> and significantly higher than that of the other three materials. In the ESR spectrum of  $\cdot\text{OH}$ , as shown in Figure 9b, the signal peak generated by B-TiO<sub>2</sub>/C<sub>3</sub>N<sub>4</sub> was the strongest. According to the analysis results, the B-TiO<sub>2</sub>/C<sub>3</sub>N<sub>4</sub> material produced the most  $\cdot\text{O}_2^-$  and  $\cdot\text{OH}$  in the visible light photocatalytic system, so it had a better photocatalytic effect.

Otherwise, the XPS characterization showed that the B element in B<sub>2</sub>O<sub>3</sub> entered the TiO<sub>2</sub> crystal structure. Therefore, in order to analyze the structural composition of B-TiO<sub>2</sub> and B-C<sub>3</sub>N<sub>4</sub>, the conduction band relationship of the forbidden band width of B-TiO<sub>2</sub> and B-C<sub>3</sub>N<sub>4</sub> was analyzed. The specific results are shown in Figure 10a.

The photocatalytic reaction mechanism of B-TiO<sub>2</sub>/C<sub>3</sub>N<sub>4</sub> composite material was deduced according to the radical trapping experiment. As shown in Figure 10b, under visible light conditions, the conduction band position of B-C<sub>3</sub>N<sub>4</sub> was  $-0.88$  eV, which was more negative than that of B-TiO<sub>2</sub> ( $-0.31$  eV) and E<sub>0</sub> ( $\text{O}_2/\cdot\text{O}_2^- = -0.33$  eV). The electrons could be captured by O<sub>2</sub> to form  $\cdot\text{O}_2^-$  and finally formed H<sub>2</sub>O<sub>2</sub> on the surface of the material. The holes were trapped by H<sub>2</sub>O and OH<sup>-</sup> in the valence band of B-TiO<sub>2</sub> to form hydroxyl radicals ( $\cdot\text{OH}$ ). These species are vital for photocatalytic degradation of organic pollution. Meanwhile, it can be determined that the B-TiO<sub>2</sub>/C<sub>3</sub>N<sub>4</sub> composite material formed a Z-type heterostructure [43,44].

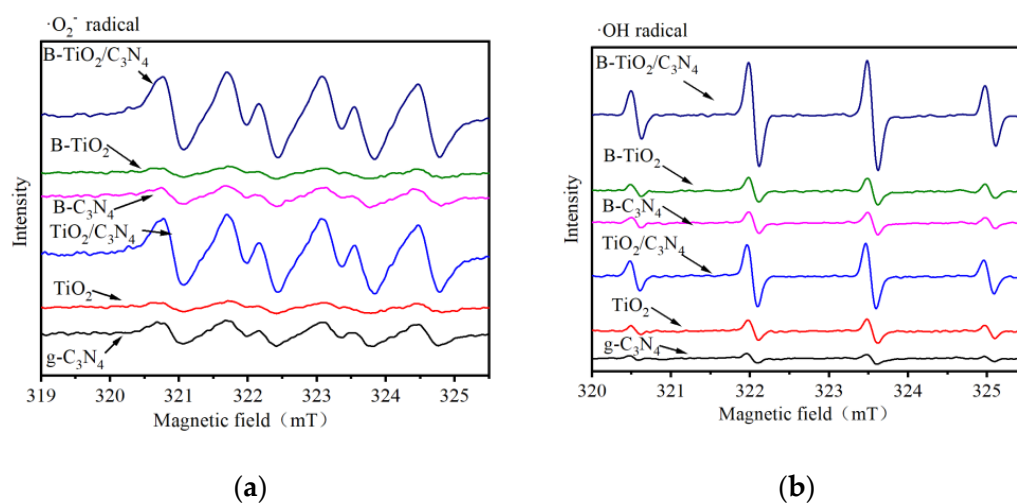


**Figure 9.** Spectrum of DMPO spin trapping ESR of different materials (a) DMPO- $\text{O}_2^{\cdot -}$  and (b) DMPO-OH.

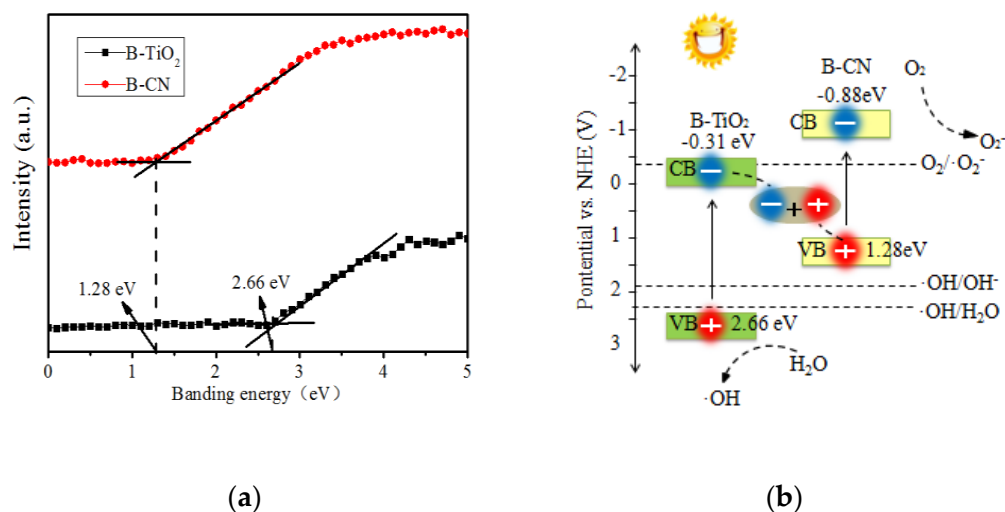


**Figure 10.** The photocatalytic reaction mechanism of B-TiO<sub>2</sub>/C<sub>3</sub>N<sub>4</sub>: (a) The VB XPS of B-TiO<sub>2</sub> and B-CN; (b) Scheme of proposed mechanism for degradation of B-TiO<sub>2</sub>/C<sub>3</sub>N<sub>4</sub>.

#### 4. Conclusions

Herein, B-TiO<sub>2</sub>/C<sub>3</sub>N<sub>4</sub> composites were prepared by modifying Z-type heterostructured TiO<sub>2</sub>/C<sub>3</sub>N<sub>4</sub> composites using the molten reaction environment created by B<sub>2</sub>O<sub>3</sub>. The physical-chemical properties of B-TiO<sub>2</sub>/C<sub>3</sub>N<sub>4</sub> composites prepared at different temperatures were analyzed by various characterization methods. Through characterization, it was found that the addition of B<sub>2</sub>O<sub>3</sub> effectively increased the specific surface area of TiO<sub>2</sub>/C<sub>3</sub>N<sub>4</sub> materials, thereby increasing the active sites for adsorption and photocatalysis. Crystal analysis showed that the modification of TiO<sub>2</sub>/C<sub>3</sub>N<sub>4</sub> by B<sub>2</sub>O<sub>3</sub> simultaneously doped B element into the TiO<sub>2</sub> lattice and g-C<sub>3</sub>N<sub>4</sub>, which helped to inhibit the recombination of electron holes and improved the photocatalytic activity. At the same time, the doping of B element expanded the  $\pi$ -conjugated system of the g-C<sub>3</sub>N<sub>4</sub> material, which is beneficial for the improvement of MB adsorption performance. Above all, this paper started with consideration of the two aspects of improving the adsorption capacity and photocatalytic oxidation capacity of the material and integrated the preparation, characterization, and adsorption–degradation mechanism analysis of the material, providing theoretical support and experimental basis for research on the synergistic removal of pollutants by adsorption and photocatalysis.

**Supplementary Materials:** The following supporting information can be downloaded at: <https://www.mdpi.com/article/10.3390/ijerph19148683/s1>, Table S1: Comparison of MB removal rate of different materials, Figure S1: MB removal efficiency of several materials: TiO<sub>2</sub>, g-C<sub>3</sub>N<sub>4</sub>, B-TiO<sub>2</sub>, B-C<sub>3</sub>N<sub>4</sub>, TiO<sub>2</sub>/C<sub>3</sub>N<sub>4</sub>, B<sub>2</sub>-C<sub>3</sub>N<sub>4</sub>/TiO<sub>2</sub> and B-TiO<sub>2</sub>/C<sub>3</sub>N<sub>4</sub>, Figure S2: MB removal efficiency of B-TiO<sub>2</sub>/C<sub>3</sub>N<sub>4</sub> prepared with different doping amount, Figure S3: N<sub>2</sub> adsorption-desorption curves of B-TiO<sub>2</sub>/C<sub>3</sub>N<sub>4</sub> materials at different temperatures, Figure S4: XRD (X-ray diffraction) patterns of B<sub>2</sub>O<sub>3</sub> and B-TiO<sub>2</sub>/C<sub>3</sub>N<sub>4</sub>-2 Series materials, Figure S5: FT-IR spectra for different temperature B-TiO<sub>2</sub>/C<sub>3</sub>N<sub>4</sub>, Figure S6: XPS spectra of B-TiO<sub>2</sub>/C<sub>3</sub>N<sub>4</sub> material (a)B1s, (b)C1s, (c) N1s, (d) Ti2p and (e) O1s, Figure S7. The Diffuse reflectance spectra for different temperature B-TiO<sub>2</sub>/C<sub>3</sub>N<sub>4</sub>, Figure S8. Synthesis path of B-TiO<sub>2</sub>/C<sub>3</sub>N<sub>4</sub> material, Figure S9. Changes of TOC in the experiment of adsorption-catalytic degradation of pollutants (a) MB (b) RhB. References [45–47] are cited in the supplementary materials.

**Author Contributions:** X.G. contributed substantially to the design of the study, the analyses, writing of the manuscript, and the original draft preparation. L.R. contributed to the project administration, funding acquisition, and verified the experimental data, replied to comments, and corrected the proof. Z.S. took responsibility for performing experiments and validation and made the figures. All authors have read and agreed to the published version of the manuscript.

**Funding:** This work was funded by grants from the National Natural Science Foundation of China (no. 51775167) and the National Major Projects of Water Pollution Control and Management Technology (no. 2017ZX07204003).

**Institutional Review Board Statement:** Not applicable.

**Informed Consent Statement:** Not applicable.

**Data Availability Statement:** Not applicable.

**Conflicts of Interest:** The authors declare no conflict of interest.

## References

1. Ratshiedana, R.; Kuvarega, A.T.; Mishra, A.K. Titanium Dioxide and Graphitic Carbon Nitride-Based Nanocomposites and Nanofibres for the Degradation of Organic Pollutants in Water: A Review. *Environ. Sci. Pollut. Res.* **2021**, *28*, 10357–10374. [[CrossRef](#)] [[PubMed](#)]
2. Xie, K.; Fang, J.; Li, L.; Deng, J.; Chen, F. Progress of Graphite Carbon Nitride with Different Dimensions in the Photocatalytic Degradation of Dyes: A Review. *J. Alloys Compd.* **2022**, *901*, 163589. [[CrossRef](#)]
3. Hu, C.; Tu, S.; Tian, N.; Ma, T.; Zhang, Y.; Huang, H. Photocatalysis Enhanced by External Fields. *Angew. Chem. Int. Ed.* **2021**, *60*, 16309–16328. [[CrossRef](#)] [[PubMed](#)]
4. Ahmaruzzaman, M.d.; Mishra, S.R. Photocatalytic Performance of g-C<sub>3</sub>N<sub>4</sub> Based Nanocomposites for Effective Degradation/Removal of Dyes from Water and Wastewater. *Mater. Res. Bull.* **2021**, *143*, 111417. [[CrossRef](#)]
5. Oh, J.; Shim, Y.; Lee, S.; Park, S.; Jang, D.; Shin, Y.; Ohn, S.; Kim, J.; Park, S. Structural Insights into Photocatalytic Performance of Carbon Nitrides for Degradation of Organic Pollutants. *J. Solid State Chem.* **2018**, *258*, 559–565. [[CrossRef](#)]
6. Kuznetsov, V.N.; Serpone, N. Visible Light Absorption by Various Titanium Dioxide Specimens. *J. Phys. Chem. B* **2006**, *110*, 25203–25209. [[CrossRef](#)]
7. Xu, Q.; Zhang, L.; Cheng, B.; Fan, J.; Yu, J. S-Scheme Heterojunction Photocatalyst. *Chem* **2020**, *6*, 1543–1559. [[CrossRef](#)]
8. Ejeta, S.Y.; Imae, T. Photodegradation of Pollutant Pesticide by Oxidized Graphitic Carbon Nitride Catalysts. *J. Photochem. Photobiol. A Chem.* **2021**, *404*, 112955. [[CrossRef](#)]
9. Abe, M.; Kawashima, K.; Kozawa, K.; Sakai, H.; Kaneko, K. Amination of Activated Carbon and Adsorption Characteristics of Its Aminated Surface. *Langmuir* **2000**, *16*, 5059–5063. [[CrossRef](#)]
10. Zhou, Z.; Li, K.; Deng, W.; Li, J.; Yan, Y.; Li, Y.; Quan, X.; Wang, T. Nitrogen Vacancy Mediated Exciton Dissociation in Carbon Nitride Nanosheets: Enhanced Hydroxyl Radicals Generation for Efficient Photocatalytic Degradation of Organic Pollutants. *J. Hazard. Mater.* **2020**, *387*, 122023. [[CrossRef](#)]
11. Hossain, S.M.; Park, H.; Kang, H.-J.; Mun, J.S.; Tijing, L.; Rhee, I.; Kim, J.-H.; Jun, Y.-S.; Shon, H.K. Facile Synthesis and Characterization of Anatase TiO<sub>2</sub>/g-CN Composites for Enhanced Photoactivity under UV-Visible Spectrum. *Chemosphere* **2021**, *262*, 128004. [[CrossRef](#)] [[PubMed](#)]
12. Serpone, N. Relative Photonic Efficiencies and Quantum Yields in Heterogeneous Photocatalysis. *J. Adv. Oxid. Technol.* **1997**, *2*, 203–216. [[CrossRef](#)]
13. Yu, L.; Wang, Z.; Shi, L.; Yuan, S.; Zhao, Y.; Fang, J.; Deng, W. Photoelectrocatalytic Performance of TiO<sub>2</sub> Nanoparticles Incorporated TiO<sub>2</sub> Nanotube Arrays. *Appl. Catal. B Environ.* **2012**, *113–114*, 318–325. [[CrossRef](#)]

14. Valero-Romero, M.J.; Santaclara, J.G.; Oar-Arteta, L.; van Koppen, L.; Osadchii, D.Y.; Gascon, J.; Kapteijn, F. Photocatalytic Properties of TiO<sub>2</sub> and Fe-Doped TiO<sub>2</sub> Prepared by Metal Organic Framework-Mediated Synthesis. *Chem. Eng. J.* **2019**, *360*, 75–88. [CrossRef]
15. Kamegawa, T.; Shimizu, Y.; Yamashita, H. Superhydrophobic Surfaces with Photocatalytic Self-Cleaning Properties by Nanocomposite Coating of TiO<sub>2</sub> and Polytetrafluoroethylene. *Adv. Mater.* **2012**, *24*, 3697–3700. [CrossRef]
16. Horikoshi, S.; Serpone, N. Can the Photocatalyst TiO<sub>2</sub> Be Incorporated into a Wastewater Treatment Method Background and Prospects. *Catal. Today* **2020**, *340*, 334–346. [CrossRef]
17. Zhang, F.; Hong, B.; Zhao, W.; Yang, Y.; Bao, J.; Gao, C.; Sun, S. Ozone Modification as an Efficient Strategy for Promoting the Photocatalytic Effect of TiO<sub>2</sub> for Air Purification. *Chem. Commun.* **2019**, *55*, 3757–3760. [CrossRef]
18. Yuzer, B.; Aydın, M.I.; Con, A.H.; Inan, H.; Can, S.; Selcuk, H.; Kadmi, Y. Photocatalytic, Self-Cleaning and Antibacterial Properties of Cu(II) Doped TiO<sub>2</sub>. *J. Environ. Manag.* **2022**, *302*, 114023. [CrossRef]
19. Hossain, S.M.; Tijing, L.; Suzuki, N.; Fujishima, A.; Kim, J.-H.; Shon, H.K. Visible Light Activation of Photocatalysts Formed from the Heterojunction of Sludge-Generated TiO<sub>2</sub> and g-CN towards NO Removal. *J. Hazard. Mater.* **2022**, *422*, 126919. [CrossRef]
20. Ojha, D.P.; Karki, H.P.; Kim, H.J. Design of Ternary Hybrid ATO/g-C<sub>3</sub>N<sub>4</sub>/TiO<sub>2</sub> Nanocomposite for Visible-Light-Driven Photocatalysis. *J. Ind. Eng. Chem.* **2018**, *61*, 87–96. [CrossRef]
21. Wang, P.; Guo, X.; Rao, L.; Wang, C.; Guo, Y.; Zhang, L. A Weak-Light-Responsive TiO<sub>2</sub>/g-C<sub>3</sub>N<sub>4</sub> Composite Film: Photocatalytic Activity under Low-Intensity Light Irradiation. *Environ. Sci. Pollut. Res.* **2018**, *25*, 20206–20216. [CrossRef] [PubMed]
22. Kumar, U.; Hassan, J.Z.; Bhatti, R.A.; Raza, A.; Nazir, G.; Nabgan, W.; Ikram, M. Photocatalysis vs Adsorption by Metal Oxide Nanoparticles. *J. Mater. Sci. Technol.* **2022**. [CrossRef]
23. Bahrudin, N.N.; Nawi, M.A.; Zainal, Z. Insight into the Synergistic Photocatalytic-Adsorptive Removal of Methyl Orange Dye Using TiO<sub>2</sub>/Chitosan Based Photocatalyst. *Int. J. Biol. Macromol.* **2020**, *165*, 2462–2474. [CrossRef] [PubMed]
24. Zhu, Y.; Ji, H.; He, K.; Blaney, L.; Xu, T.; Zhao, D. Photocatalytic Degradation of GenX in Water Using a New Adsorptive Photocatalyst. *Water Res.* **2022**, *220*, 118650. [CrossRef] [PubMed]
25. Liu, M.; Zhang, D.; Han, J.; Liu, C.; Ding, Y.; Wang, Z.; Wang, A. Adsorption Enhanced Photocatalytic Degradation Sulfadiazine Antibiotic Using Porous Carbon Nitride Nanosheets with Carbon Vacancies. *Chem. Eng. J.* **2020**, *382*, 123017. [CrossRef]
26. Guo, X.; Rao, L.; Wang, P.; Zhang, L.; Wang, Y. Synthesis of Porous Boron-Doped Carbon Nitride: Adsorption Capacity and Photo-Regeneration Properties. *Int. J. Environ. Res. Public Health* **2019**, *16*, 581. [CrossRef]
27. Rodríguez-Narciso, S.; Lozano-Álvarez, J.A.; Salinas-Gutiérrez, R.; Castañeda-Leyva, N. A Stochastic Model for Adsorption Kinetics. *Adsorpt. Sci. Technol.* **2021**, *2021*, 5522581. [CrossRef]
28. Zhu, Z.; Xie, J.; Zhang, M.; Zhou, Q.; Liu, F. Insight into the Adsorption of PPCPs by Porous Adsorbents: Effect of the Properties of Adsorbents and Adsorbates. *Environ. Pollut.* **2016**, *214*, 524–531. [CrossRef]
29. She, X.; Liu, L.; Ji, H.; Mo, Z.; Li, Y.; Huang, L.; Du, D.; Xu, H.; Li, H. Template-Free Synthesis of 2D Porous Ultrathin Nonmetal-Doped g-C<sub>3</sub>N<sub>4</sub> Nanosheets with Highly Efficient Photocatalytic H<sub>2</sub> Evolution from Water under Visible Light. *Appl. Catal. B Environ.* **2016**, *187*, 144–153. [CrossRef]
30. Guo, Q.; Ma, Z.; Zhou, C.; Ren, Z.; Yang, X. Single Molecule Photocatalysis on TiO<sub>2</sub> Surfaces. *Chem. Rev.* **2019**, *119*, 11020–11041. [CrossRef]
31. Li, L.; Hong, W.B.; Yan, X.J.; Chen, X.M. Preparation and Microwave Dielectric Properties of B<sub>2</sub>O<sub>3</sub> Bulk. *Int. J. Appl. Ceram. Technol.* **2019**, *16*, 2047–2052. [CrossRef]
32. Photocatalytic Activity Enhancement of Core-Shell Structure g-C<sub>3</sub>N<sub>4</sub>@TiO<sub>2</sub> via Controlled Ultrathin g-C<sub>3</sub>N<sub>4</sub> Layer-ScienceDirect. Available online: <https://www.sciencedirect.com/science/article/abs/pii/S0926337317307403> (accessed on 20 June 2022).
33. Mozzi, R.L.; Warren, B.E. The Structure of Vitreous Boron Oxide. *J. Appl. Cryst.* **1970**, *3*, 251–257. [CrossRef]
34. Danon, A.; Stair, P.C.; Weitz, E. FTIR Study of CO<sub>2</sub> Adsorption on Amine-Grafted SBA-15: Elucidation of Adsorbed Species. *J. Phys. Chem. C* **2011**, *115*, 11540–11549. [CrossRef]
35. Quiñones, D.H.; Rey, A.; Álvarez, P.M.; Beltrán, F.J.; Li Puma, G. Boron Doped TiO<sub>2</sub> Catalysts for Photocatalytic Ozonation of Aqueous Mixtures of Common Pesticides: Diuron, o-Phenylphenol, MCPA and Terbutylazine. *Appl. Catal. B Environ.* **2015**, *178*, 74–81. [CrossRef]
36. Ahmed, T.; Ammar, M.; Saleem, A.; Zhang, H.; Xu, H. Z-Scheme 2D-m-BiVO<sub>4</sub> Networks Decorated by a g-CN Nanosheet Heterostructured Photocatalyst with an Excellent Response to Visible Light. *RSC Adv.* **2020**, *10*, 3192–3202. [CrossRef]
37. Wei, H.; McMaster, W.A.; Tan, J.Z.Y.; Cao, L.; Chen, D.; Caruso, R.A. Mesoporous TiO<sub>2</sub>/g-C<sub>3</sub>N<sub>4</sub> Microspheres with Enhanced Visible-Light Photocatalytic Activity. *J. Phys. Chem. C* **2017**, *121*, 22114–22122. [CrossRef]
38. Guo, Y.; Wang, R.; Wang, P.; Rao, L.; Wang, C. Developing a Novel Layered Boron Nitride–Carbon Nitride Composite with High Efficiency and Selectivity To Remove Protonated Dyes from Water. *ACS Sustain. Chem. Eng.* **2019**, *7*, 5727–5741. [CrossRef]
39. Zhu, J.; Chen, F.; Zhang, J.; Chen, H.; Anpo, M. Fe<sup>3+</sup>-TiO<sub>2</sub> Photocatalysts Prepared by Combining Sol–Gel Method with Hydrothermal Treatment and Their Characterization. *J. Photochem. Photobiol. A Chem.* **2006**, *180*, 196–204. [CrossRef]
40. Barkul, R.P.; Sutar, R.S.; Patil, M.K.; Delekar, S.D. Photocatalytic Degradation of Organic Pollutants by Using Nanocrystalline Boron-Doped TiO<sub>2</sub> Catalysts. *ChemistrySelect* **2021**, *6*, 3360–3369. [CrossRef]
41. Beltrán, F.J.; Aguinaco, A.; García-Araya, J.F. Kinetic Modelling of TOC Removal in the Photocatalytic Ozonation of Diclofenac Aqueous Solutions. *Appl. Catal. B Environ.* **2010**, *100*, 289–298. [CrossRef]

42. Lee, J.C.; Park, S.; Park, H.-J.; Lee, J.-H.; Kim, H.-S.; Chung, Y.-J. Photocatalytic Degradation of TOC from Aqueous Phenol Solution Using Solution Combusted ZnO Nanopowders. *J. Electroceram.* **2009**, *22*, 110–113. [[CrossRef](#)]
43. Tatykayev, B.; Chouchene, B.; Balan, L.; Gries, T.; Medjahdi, G.; Girot, E.; Uralbekov, B.; Schneider, R. Heterostructured g-CN/TiO<sub>2</sub> Photocatalysts Prepared by Thermolysis of g-CN/MIL-125(Ti) Composites for Efficient Pollutant Degradation and Hydrogen Production. *Nanomaterials* **2020**, *10*, 1387. [[CrossRef](#)] [[PubMed](#)]
44. Karpuraranjith, M.; Chen, Y.; Rajaboopathi, S.; Ramadoss, M.; Srinivas, K.; Yang, D.; Wang, B. Three-Dimensional Porous MoS<sub>2</sub> Nanobox Embedded g-C<sub>3</sub>N<sub>4</sub>@TiO<sub>2</sub> Architecture for Highly Efficient Photocatalytic Degradation of Organic Pollutant. *J. Colloid Interface Sci.* **2022**, *605*, 613–623. [[CrossRef](#)] [[PubMed](#)]
45. Feng, J.; Chen, T.; Liu, S.; Zhou, Q.; Ren, Y.; Lv, Y.; Fan, Z. Improvement of g-C<sub>3</sub>N<sub>4</sub> Photocatalytic Properties Using the Hummers Method. *J. Colloid Interface Sci.* **2016**, *479*, 1–6. [[CrossRef](#)]
46. Kwon, D.; Kim, J. Silver-Doped ZnO for Photocatalytic Degradation of Methylene Blue. *Korean J. Chem. Eng.* **2020**, *37*, 1226–1232. [[CrossRef](#)]
47. Mo, Z.; She, X.; Li, Y.; Liu, L.; Huang, L.; Chen, Z.; Zhang, Q.; Xu, H.; Li, H. Synthesis of g-C<sub>3</sub>N<sub>4</sub> at Different Temperatures for Superior Visible/UV Photocatalytic Performance and Photoelectrochemical Sensing of MB Solution. *RSC Adv.* **2015**, *5*, 101552–101562. [[CrossRef](#)]